Wuhan MST radar: Technical features and Validation of wind observations

Lei Qiao[1,2], Gang Chen[2], Shaodong Zhang[2], Qi Yao[3], Wanlin Gong[2], Mingkun Su[1],
Feilong Chen[4], Erxiao Liu[1], Weifan Zhang[2], Huangyuan Zeng[2], Xuesi Cai[1], Huina Song[1],
5   Huan Zhang[1], Liangliang Zhang[1]

[1] Communication Engineering School, Hangzhou Dianzi University, Hangzhou 310018, China
[2] Electronic Information School, Wuhan University, Wuhan 430072, China
[3] Nanjing Research Institute of Electronic Technology, Nanjin 210013, China
[4] Information Engineering School, Nanchang Hangkong University, Nanchang 330063, China

10   *Correspondence to*: Gang Chen (g.chen@whu.edu.cn)

Abstract. The Wuhan MST radar is a 53.8 MHz monostatic Doppler radar, located in Chongyang, Hubei Province, China, which has the capability to observe the dynamics of the mesosphere-stratosphere-troposphere region in the subtropical latitudes. The radar system has an antenna array of 576 Yagi antennas, and the maximum peak power is 172 kW. The Wuhan MST radar is efficient and cost-effective, which employs simplifier and more flexible architecture. It includes 24 big TR
15   modules, and the row/column data port of each big TR module connects 24 small TR modules via the corresponding row/column feeding network. Each antenna is driven by a small TR module with peak output power of 300 W. The arrangement of the antenna field, the functions of the timing signals, the structure of the TR modules, and the clutter suppression procedure are described in detail in this paper. We compared the MST radar observation results with other instruments and related models in the whole MST region for validation. Firstly, we made a comparison of the Wuhan MST
20   radar observed horizontal winds in the troposphere and low stratosphere with the radiosonde on 22 May 2016, as well as the ERA-interim data sets (2016 and 2017) in the long term. Then, we made a comparison of the observed horizontal winds in the mesosphere with the meteor radar and the HWM-07 model in the same way. In general, good agreements can be obtained, and it indicates that the Wuhan MST is an effective tool to measure the three-dimensional wind fields of the MST region.

1 Introduction

25   The mesosphere-stratosphere-troposphere (MST) radars has been used for studying the dynamics of the lower and middle atmosphere up to 100 km altitude for several decades (Hocking et al., 2011), since Woodman and Guillen observed radar echoes from the stratospheric and mesospheric heights with the Jicamarca radar in 1970s (Woodman et al., 1974). In general, large antenna array is employed by these MST radars to measure the weak echoes scattered by the turbulence (Green et al., 1979). Many MST radars have been developed world-wide by different countries and groups, and the MST community plays
30   a significant role in technique sharing. According to the antenna array shape, the existing MST radar in the world can be

divided into two types: the square array arranging the elements in a square gird and the circular array arranging the elements in a triangular grid. The MST radars using the square array mainly include the Jicamarca radar (Woodman et al., 1974), the Sousy radar (Schmidt et al., 1979), the Poker Flat radar (Balsley et al., 1980), the Esrange MST radar (Chilson et al., 1999), the Gadanki radar (Rao et al., 1995), the Chung-Li radar (Rottger et al., 1990; Chu et al., 2009) and the NERC MST radar

35 (Vaughan et al., 2002; Hooper et al., 2013). The MST radars using the circular array include the MU radar (Fukao et al., 1985; Kawahigashi et al., 2017), the EAR radar (Fukao et al., 2003), the MAARSY radar (Latteck et al., 2012) and the PANSY radar (Sato et al., 2014).

Until 2008, the Wuhan MST radar and Beijing MST radar began to construct with the support of Meridian Project of China (Wang, 2010). We have introduced the two MST radars of Chinese Meridian project in 2016 (Chen et al., 2016). This

40 paper briefly introduced the antenna array of the Beijing and Wuhan MST radars and their preliminary observations. The two MST radars work more than 280 days every year and their data can be freely accessed in the data center for the Meridian Project (http://159.226.22.74/). Thus, the radar system and their data are gained extensive attention and we have received many letters inquiring about the details of the radio system, as well as the data format and reliability. Therefore, we plan to write a new article in response to the readers' and users' demand, who want to build a low-cost MST radar or apply the data

45 of the MST radars of Chinese Meridian project. The paper presents more details of the Wuhan MST radar including some optimized circuits, as well as its recorded data.

The Wuhan MST radar is located in Chongyang, Hubei Province, China (29.5°N, 114.1°E). The location is far away from the bustling city, so as to better avoid interference by radio noise. Considering this is China's first attempt to develop its own MST radar, the radar station is not selected in some areas of great difficulty in construction, such as equatorial low latitudes,

50 polar regions and plateaus. Chongyang is located in the central plain of China, which is an appropriate choice. As one of few MST radars in the midlatitudes, it can be one important member of the global MST radars. In addition to the scientific research goals, the Chongyang station also serves as a students' training base for the practice of radar technologies and meteorological applications. The Wuhan MST radar was completed preliminarily in 2011. The system was upgraded in 2016, and the TR modules were updated for better stability and better detection capability. The facility costs only about

55 $1,000,000.00, which is far lower than the high cost of other MST radars. However, it provides an average power aperture product (PAP) product of 3.2×10^8 Wm^2. Considering the balance of system performance and project implementation, simpler and more flexible architectures are applied in the system.

The first aim of the present paper is to introduce the technical features of the Wuhan MST radar. In particular, the antenna field, the timing signal, the TR module, the digital receiver and the clutter suppression will be discussed in detail. The

60 second aim of this paper is to present the the recorded data and compared with the wind fields recorded by other instruments and related models for validation.

2 Technical features

 ## 2.1 General description

The Wuhan MST radar is arranged in a 24 × 24 matrix with a side length of 96 m, which consists of 576 Yagi antennas. Each antenna is driven by an individual small TR module (300 W). According to the antenna radiation pattern, the beam width is 3.2°. The shortest width of the subpulse is 1 µs to satisfy the requirement for a maximum range resolution of 150 m. The radar system allows very high flexibility of waveform parameter for different detection modes (low mode, middle mode, and high mode). The basic specifications of the Wuhan MST radar are in Table 1. The hardware of the Wuhan MST radar consists mainly of five subsystems: the antenna array, the TR module, the radar controller, the digital transceiver, and the signal processor. Fig. 1 shows the schematic block diagram of the system.

Table 1. Specifications of the Wuhan MST radar

Parameter	Value
Location	29.51°N, 114.13°E
Operating frequency	53.8 MHz
Observation mode	Low mode (3.5-12 km)
	Middle mode (10-25 km)
	High mode (60-85 km)
Antenna	
Antenna type	24×24 Yagi antennas (VSWR ≤ 1.3)
Aperture	Square with a side of 96 m
Beam width	3.2°
Gain	32.8 dBi
Beam azimuth angle	0°, 90°, 180°, 270° (oblique); 0° (vertical)
Beam zenith angle	0-20° with a step size of 1°
Transmitter	
Peak power	~172 kW
Number of TR modules	576
Single TR module's power	300 W
Pulse width	1-512 µs
Receiver	
Type	Direct digitization structure
Pulse compression	Complementary code (16 or 32 bits)
Noise figure	3.7 dB (small TR module)
Dynamic	65 dB
Receiver sensitivity	-110.3 dBm
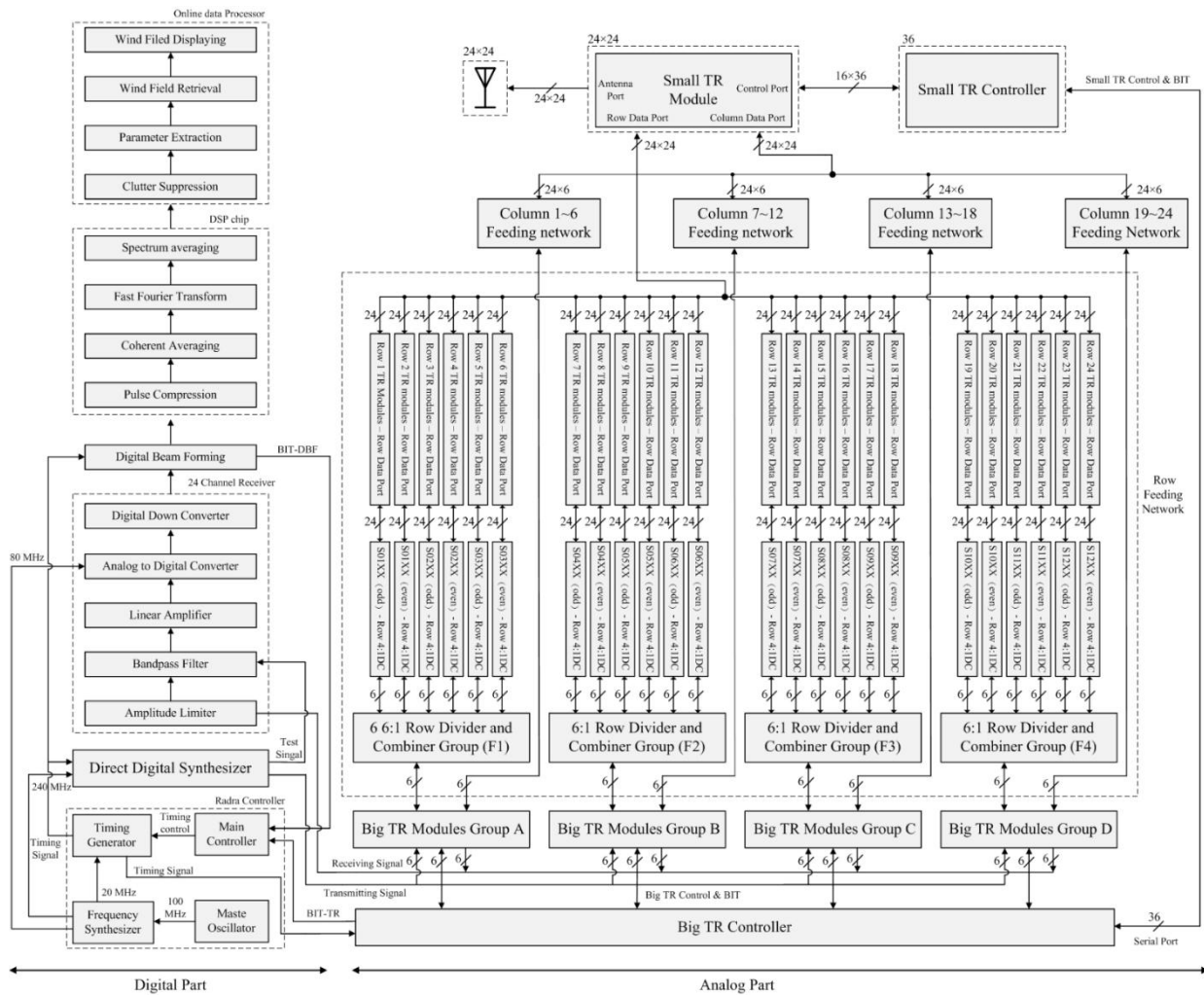
Figure 1. Schematic block diagram of the Wuhan MST radar located in Wuhan, China. The small TR module controllers, the small TR modules, the feeding network and the antenna array are installed in the antenna field. Other modules are installed in the observation house.

The signal scattered by 'refractive index irregularities' is received by the antenna array, then sent to the TR module by the feeding network. The TR module includes 24 big TR modules installed in the observation house and 576 small TR modules installed in the shelters. The big TR controller receives the timing signal from the timing generator in the radar controller by parallel port. The big TR controller converts the timing signal into multiplex signals to control the 24 big TR modules. At the same time, the BIT-TR signal is sent to the main controller to monitor the condition of the big TR module. The big TR controller also handles communication with 36 small TR module controllers over twisted-pair, and each big TR module controller corresponds to 16 small TR modules. The row data port in the big TR module connects 24 small TR modules in a row of the antenna array via the row feeding network, while the column data port connects 24 small TR modules in a column via the column feeding network.

The radar controller consists of a master oscillator, a frequency synthesizer and a control timing generator and a main controller. The master oscillator generates the reference clock of 100 MHz. Then, the frequency synthesizer generates the sampling clock of 80 MHz, the direct digital synthesizer (DDS) clock of 240 MHz, and the control reference clock of 20 MHz. Combined with the reference clock of 20 MHz and the commands from the main controller, the control timing generator generates various timing signals for radar control.

The digital transceiver consists of the DDS module, and the 24-channel receiver. The DDS module is used to generate the binary-phase-coded continuous wave for transmitting and the test signal for channel calibration. The 24-channel receiver includes the amplitude limiter, the bandpass filter, the linear amplifier, the analog-to-digital converter (ADC) and the digital down converter (DDC). The amplitude and phase weight algorithm is realized in the digital beam forming (DBF) module.

The data processing implemented in the digital signal processing (DSP) chip involves pulse compression, coherent averaging, fast Fourier transform (FFT), and spectrum averaging. Then, the output of the DSP chip is transferred to the online data processor by a peripheral component interconnect (PCI) bus. The main functions of the online data processor are clutter suppression, parameter extraction, wind field retrieval and wind field displaying. Eventually, the product data of the wind field in the troposphere, lower stratosphere, and mesosphere is produced.

2.2 Antenna field
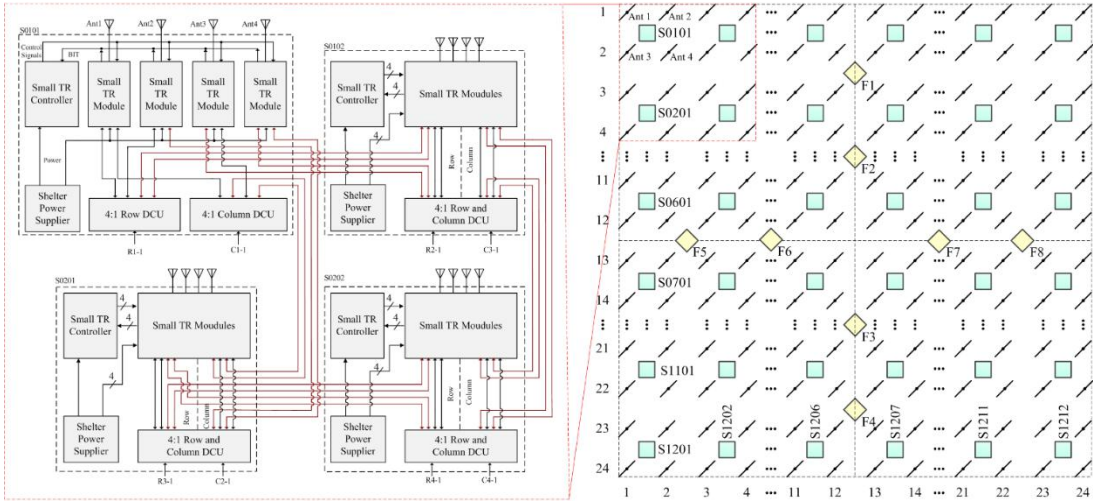
Figure 2. Arrangement of the Wuhan MST radar antenna field and inter connections of four surrounding shelters.

Fig. 2 shows the arrangement of the Wuhan MST radar antenna field. The Yagi antennas are arrayed on grids of squares about 4 m on a side, and this element spacing allows no grating lobe beam scanning up to an angle of about 24° from zenith. The voltage standing wave ratio (VSWR) of the antenna is less than 2.5.

As shown in the right part of Fig. 2, there are 144 shelters mounted at regular intervals, and each one consists of 4 small TR modules, a 4:1 row divider/combiner unit (DCU), a 4:1 column DCU, and a power supplier and a small TR controller. It

110 should be pointed out that the 36 small TR controllers are located in the shelters of odd rows and columns. The eight yellow boxes, labeled as F1-F8, represent the row feeding boxes (F1-F4) and the column feeding boxes (F5-F8). Each feeding boxes contains six 6:1 DCUs, and each one feeds four 4:1 DCUs in the shelters. The DCUs in the row/column feeding boxes are all fed by the big TR modules in the observation house, and the row or column drive state is switched by the control signal. The row/column data from the 24 big TR module feeding the 6:1 row/column DCUs is labeled as R1-R24/C1-C24.

115 As illustrated by the red box in the right part of Fig. 2, there are four shelters (S0101, S0102, S0201, S0202) and the surrounding antennas. The left part of Fig. 2 shows the inter connections of the shelters, and the lines of different shelters are red for easy review. In the shelter S0101, the row DCU is fed by R1-1, which represents the first divided signal of R1. The other 4 ports of the row DCU connect to the row data ports of small TR module 1 and 2 in S0101 and S0102 respectively. Similarly, the column DCU is fed by C1-1, and the other 4 ports connect to small TR module 1 and 3 in S0101 and S0201

120 respectively. By analogy, the row/column DCUs of the shelter S0102, S0201, and S0202 connect to proper data ports of the small TR modules. With this system configuration, the beam can be steered to north-south direction in the row drive state and east-west direction in the column direction. The antennas are aligned in the northwest-southeast direction for symmetrical radiation pattern. The beams are usually steered to five directions (vertical, north, south, east, west) with off-zenith angles of 15°.

125 The feeding network of the Wuhan MST radar uses feeding cables of equal length. In this situation, the feeding cables of different channels have stable characteristics, which need no compensation. The big TR modules, the 6:1 dividers and combiners, the 4:1 dividers and combiners , and the antennas are connected via coaxial cable (-3dB/100m). The feeding cables of above modules are 100 m, 50 m, 10 m, and 7m respectively. Therefore, the feeding line loss from the TR module in the observation house to the end antenna of the array is about 5 dB.

130 **2.3 Timing signal**
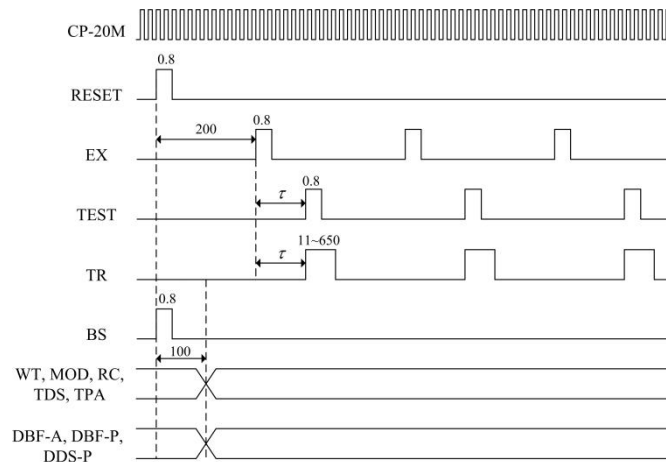
Figure 3. Timing diagram of the signals for radar operation.

Table 2. Description of control signals.

Signal	Function	Description
WT	Work/Test	0: Test 1: Work
MOD	Mode control	000~111: Low mode 1, Low mode 2, Low mode 3, Middle mode 1, Middle mode 2, High mode 1, High mode 2, High mode 3
RC	Row/Column switch	0: Row 1: Column
TDS	Test signal Doppler shift	000~111: 0, 1, 2, 5, 10, 20, 50, 100 Hz
TPA	Test signal power attenuation	000~1111: 7, 15, 23, 31, 38, 46, 54, 62 dB
DBF-A	DBF amplitude weighting coefficient	0000~1111: 32 sets of amplitude weighting coefficient
DBF-P	DBF phase weighting coefficient	00000~11000: 41 sets of DBF phase weighting coefficient(-20°~20°)
DDS-P	DDS phase weighting coefficient	00000~11000: 41 sets of DDS phase weighting coefficient(-20°~20°)

135

All timing signals for radar operation are generated by the timing generator in the radar controller. Fig. 3 presents the timing diagram of the signals at the radar controller. They are generated from the reference clock signal of CP-20M. The RESET signal is used to activate the timing generator. The excitation (EX) signal is used to generate the pulse repetition period (PRP), and the value is different according to different detection modes. The EX signal is 200 µs later than the RESET signal. The sign τ is the delay of the TEST signal and the TR signal compared to the EX signal. The delay can be adjusted by software, and the rang is from half period of clock ahead to half period of clock delay. The transmitted pulse width of the TR signal is from 11 µs to 650 µs, which is related to the compressed pulse width and the coding scheme. The beam switch (BS) signal controls the switching of the vertical beam and four oblique beams, and it is synchronised with the RESET signal.

Besides the transmitting and receiving timing signals, the radar controller also generates the control signals for system control, which are shown in the last two lines of Fig. 3. It should be pointed out that the control signals are valid 100 µs after the RESET signal rising edge. The different control signals are listed in Table 2. The work/test (WT) signal causes the system to operate in work mode or test mode. The test mode is applied for digital receive channels calibration. The mode control (MOD) signal is used to select the observation mode: low mode (troposphere), middle mode (stratosphere), and high mode (mesosphere). The low mode 1, middle mode 1, and high mode 1 are usually selected under normal operating conditions. The corresponding Doppler resolution and radar scanning time are 0.53 m/s and 5 min. The parameters of the

other observation modes can be set flexibly for applications of high Doppler resolution. The row/column switch (RC) signal is used to control the R/C switch in the small TR modules and big TR modules. The test signal Doppler shift (TDS) signal sets the test signal to establish different value of Doppler shift, which servers the digital channel calibration. The test signal power attenuation (TPA) signal controls the attenuation coefficient of the test signal, so as to prevent damage to the digital receiver. The DBF amplitude weighting coefficient (DBF-A) signal and the DBF phase weighting coefficient (DBF-P) signal are used for beam forming in the DBF module. The DDS phase weighting coefficient (DDS-P) signal causes the DDS to generate the beams of different zenith angles with a step size of 1°, and the maximum angle is 20°.

2.4 TR Module

(a)

(b)
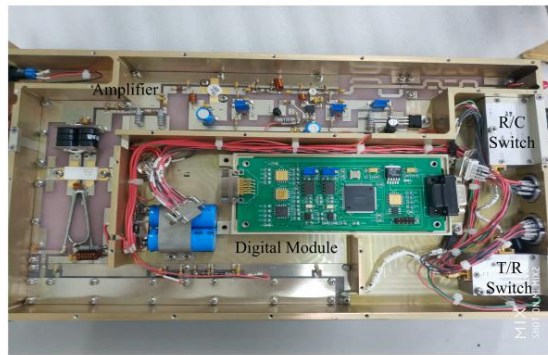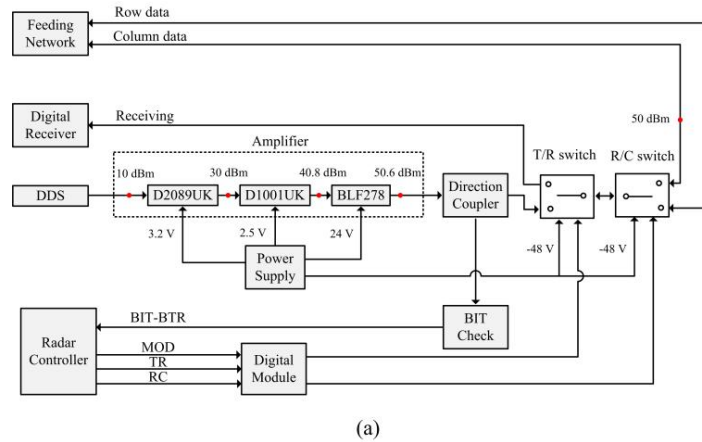
Figure 4. Block diagram (a) and photograph (b) of the big TR module.

Block diagram and photograph of the big TR module is shown in Fig. 4. The big TR module amplifies the DDS output (53.8 MHz) supplied from the digital transceiver module, and feeds it to the feeding network. This module consists of a three-stage amplifier with a gain of 40.6 dB. The D2089UK and D1001UK are employed in the first and second power amplifier stage, whose drain-source voltage is 3.2 V and 2.5 V respectively. They are metal gate RF silicon field effect transistors (FET) with

different power output. The DDS output (10 dBm) is amplified to 30 dBm in the first stage, while the first stage output is amplified to 40.8 dBm in the second stage. The push-pull power metal oxide semiconductor (MOS) transistor BLF278 is employed in the final stage with a gain of 9.8 dB, whose drain-source voltage is 24 V. Built-in test (BIT) technique is adopted to detect VSWR and power information of the amplifier output (50.6 dBm) via a directional coupler. The

170 information is not only used to monitor status of the big TR module, but also avoid damage to the amplifier. The insertion loss of the T/R switch and R/C switch in the big TR module is about 0.3 dB. Therefore, the total output becomes 50 dBm.

The control signals transferred from the big TR controller are transformed over twisted-pair for better transmission ability. The TR signal (differential signal) is converted into a single ended signal by the differential converter, and then it controls the R/C switch to realize transformation of row/column. The differential receiver chip DS96F173 is used as the differential

175 converter, which allows operating at high speed while minimizing power consumption. The TR signal controls the T/R switch to receive the signal from the row/column data port, or transmit the amplifier output to the row/column data port. The MOD signal is transferred to the digital module, so as to generate timing signals to control the T/R switch and R/C switch for different observation modes. The recovery time of the two switches is less than 5μs, which reaches the allowable level. The power supply provides -48 V for the two switches. It should point out that the differential converter is involved in the digital

180 module, as shown in Fig. 4(b).
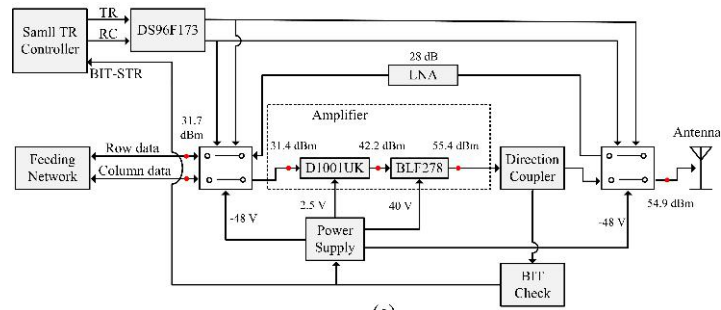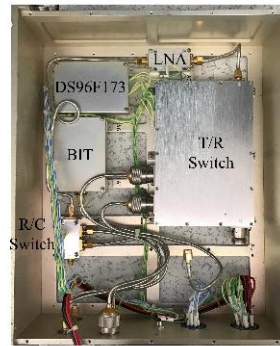
Figure 5. Block diagram (a) and photograph (b) of the small TR module.

Block diagram and photograph of the small TR module are shown in Fig. 5. The small TR module consists of various submodules: an amplifier, a T/R switch, a R/C switch, a BIT module, and a differential receiver. Each row/column signal is divided equally into 24 signals in the feeding network. Considering the attenuation of the dividers and cables (100 m cable: -3 dB; 1:6 divider: -7.78 dB; 50m cable: -1.5 dB; 1:4 divilder: -6.02 dB), the transmitting signal from the big TR module is reduced to 31.7 dBm. Then the signal is transmitted through a low power R/C switch with 0.3 dB insertion loss. A two-stage amplifier in the small TR module amplified the signal from 31.4 dBm up to 55.4 dBm, and the drain-source voltage of BLF278 is 40V with a gain of 13.2 dB. Then, a band pass filter centered on 53.8 MHz is provided for spurious emission suppression. The T/R switch in the small TR module has an insertion loss of about 0.5 dB and provides an isolation of 60 dB. Ultimately, the output of the small TR module is about 300 W, and the signal is fed to the Yagi antenna via a 7m coaxial cable. The low-noise amplifier (LNA) in the receiving channel is a 53.8 MHz tuned amplifier with a gain of 28 dB and a bandwidth of 1 MHz.

The two switches embedded in the small TR module allow the controller to select proper signaling pathway, and they are both controlled by two control signals from the small TR radar controller. The small TR module is the easiest damaged part in the system. Therefore, it needs to be repaired every year. As shown in Fig. 5(b), the small TR module adopts the modular design, which is convenient for maintenance.

2.5 Digital Transceiver

The digital-up-converter (DUC) chip AD9957 is used in the DDS module, which has 1 Gsps internal clock speed with 18-bit IQ data path and 14-bit digital-to-analog converter (DAC). The 16-bit or 32-bit complementary code with different pulsewidth (1μs, 4μs and 8μs) are generated by the DDS module, as well as the test signal. The passive calibration algorithm is used for amplitude and phase calibration of the 24 channels in the receiver. The test signal can be set with different value of Doppler shift, and is divided into 24 channel signal by the divider. The intrinsic amplitude and phase differences among channels can be extracted by comparing the output of each channel. Then, the amplitude and phase calibration factors are stored in the register. Through correction, the receiver has an amplitude consistency of -0.5-0.5 dB and a phase consistency of -2°-2° after calibration.

In the receiver, the signal firstly goes through the amplitude limiter for protection of the receiver, the linear amplifier with 50 dB gain, the bandpass with the center frequency of 53.8 MHz and bandwidth of 1 MHz, respectively. Then, the signal is sampled by the LTC2208 with 80 Msps clock rate. It is an ADC with 16-bit resolution, maximum 130 Msps and 100 dB spurious free dynamic range (SFDR). By directly bandpass sampling, the received signal is aliased to 26.2 MHz. The DDC unit is integrated in the FPGA, which is made up of the numerically controlled oscillator (NCO), the cascade integrator comb (CIC) filter, and the finite impulse response (FIR) filter. In general, the frequency output of the NCO is 26.2 MHz, the bandwidth of the FIR filter is 1 MHz, and the total decimation value is 80. Eventually, the in-phase (I) component and quadrature phase (Q) component with 1 MHz are transformed to the digital beam forming module for further processing.

2.6 Clutter suppression
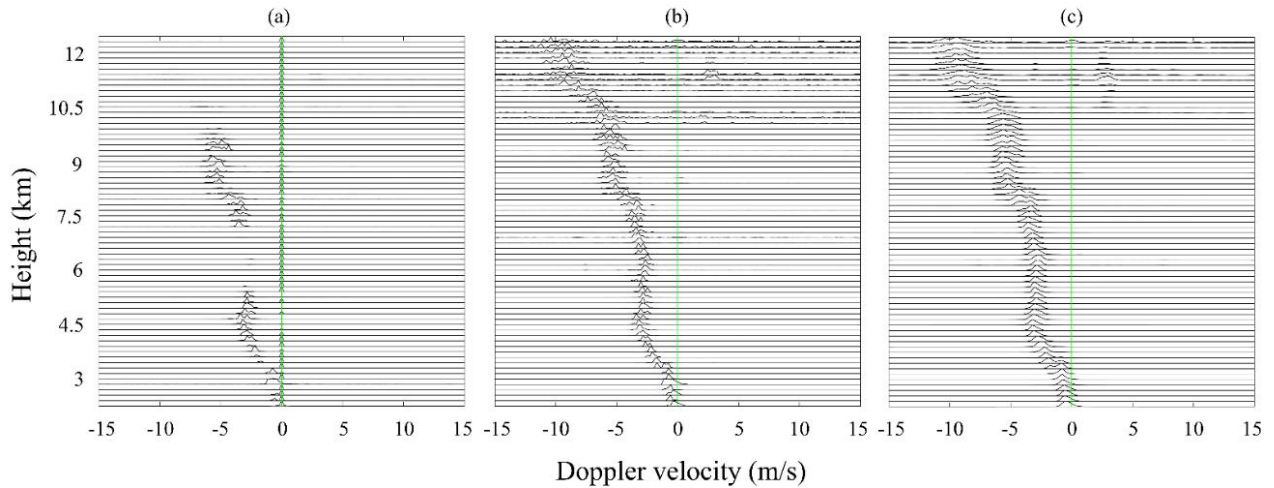
Figure 6. Comparison of the original (a), ground clutter suppressed (b), and filtered (c) Doppler spectrum.

220

The clutter suppression is carried out in the online data processor. Kumar et al. identified the turbulence echo in the multipeaked VHF radar spectra during the precipitation, and here we mainly aimed at ground clutter and high frequency interference during fair weather. Ground clutters from surrounding mountains, trees, and buildings can severely degrade parameter estimates of the turbulence (Schmidt et al., 1979). It is because the weak echoes from the clear air are easy to be

225 contaminated for the lager amplitude of the ground clutters. From the perspective of radar infrastructure, the construction of fence is an effective method to isolate ground clutter, e.g. the 10 m height MU radar fence for ground clutter prevention (Rao et al., 2003). The fence is also constructed for the Wuhan MST radar, but there are still some ground clutters in the echoes. Therefore, ground clutter suppression is an essential step for signal processing. The ground clutter echoes have narrow central peak near zero frequency with small temporal changes, and are weakened with increasing altitude.

230 Fig. 6 shows the processing procedure of the Doppler spectra recorded by the east beam in the low mode. Note that the Doppler spectra at the range gates is normalized. It can be seen form Fig. 6(a) that the desired signals are severely biased by the ground clutters. As shown in Fig. 6(b), after the ground clutter suppression, the ground clutters near zero frequency are rejected effectively, and the weak signals appears at heights of 5.4-7.05 km and 9.75-12 km. The median filter is applied to remove the high frequency interference at each range gate. As shown in Fig. 6(c), the high frequency interferences decrease,

235 and the power spectra qualities are improved obviously.

 3 Validation of wind observations

3.1 Modes of operation
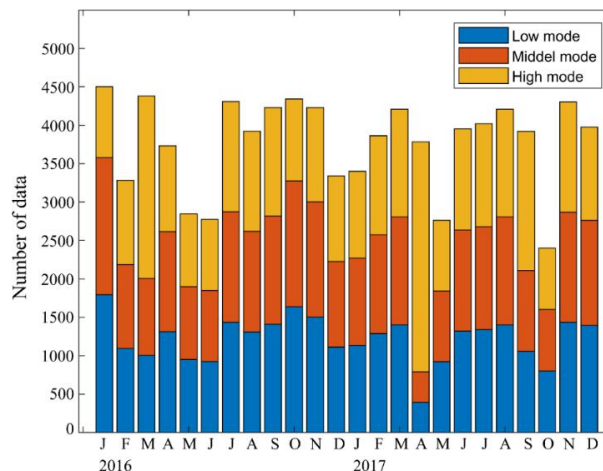
Figure 7. The monthly total number of the Wuhan MST radar data in three observation modes during January 2016 to December 2017. Blue for low mode, red for middle mode, and orange for high mode.

245

The Wuhan MST radar is used for the standard observations of the troposphere, lower stratosphere, and mesosphere in three observation modes: low mode (about 3.5-12 km), middle mode (about 10-25 km) and high mode (about 60-85 km). Height resolution is 150 m for the low mode, 600 m for the middle mode, and 1200 m for the high mode. Under the normal operation, the system usually works in each mode for 5 min in sequence, then takes a break for 15 min. Hence, the wind data

250 for each mode has 30 min temporal resolution. The Wuhan MST radar is in good running condition during the full-time unattended operation from January 2016 to December 2017. Because of the system failures or external disturbances, severe interference may appear in some data (about 1%). After removing the data with severe interference, the valid data set is present here to demonstrate the performance of the radar. Fig. 7 shows the monthly total number of the Wuhan MST radar data in low, middle and high modes. According to Fig. 7, the number of the radar data in most months exceeds 3000, except

255 March 2016, March 2017 and October 2017 during maintenance. On average, the number of daily-mean data is 41 in low mode, 41 in middle mode, and 44 in high mode. In addition, the Wuhan MST radar took more observations of the mesosphere in March 2016 and April 2017. Therefore, the data set of the two years provides comprehensive and effective coverage of the troposphere, stratosphere and mesosphere observations.

260

3.2 Data acquisition
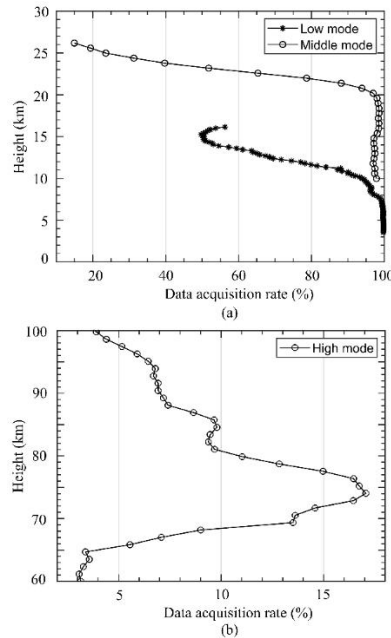
Figure 8. The average data acquisition rate from the Wuhan MST radar in low, middle (a) and high (b) observation modes during January 2016 to December 2017.

Data acquisition rate is one of the most important index to describe the MST radar performance, which is calculated using the relation: 100 × number of samples with valid horizontal wind data / total number of samples (Kumar et al., 2007). The horizontal wind velocity is estimated by the radial velocity of the four inclined beams through the use of Doppler beam swinging (DBS) technique (Anandan et al., 2001). If any one of the inclined beams has serious interference or lower signal-to-noise (SNR), which led to failure of the horizontal wind velocity inversion, then the samples are judged to be invalid. Fig. 8(a) shows the profile of total data acquisition in the low and middle mode during January 2016 to December 2017. In the low mode, the data acquisition rate remains >90% at heights of 3.5-10 km, and then decreases rapidly to 50% at height of 15 km. Note that the profile of low mode clearly shows a reversal at heights of 14-16 km corresponded to the tropopause (Chen et al., 2019). In the middle mode, the data acquisition rate remains >90% at heights of 10-20 km, and then decreases rapidly to 19% at height of 25 km. Therefore, the connection height of the low mode and middle mode is usually selected at height of 10 km for optimal data acquisition. In some situations which require high range resolution, the data acquisition rate (>50%) of the low mode is also available for the heights of 3.5-16 km.

As shown in Fig. 8(b), the data acquisition rate of the high mode is mainly concentrated at heights of 66-86 km with a maximum up to 17%, which is much lower than that of the low and middle modes. One reason is that the internal scales of neutral air turbulence in the mesosphere are mostly larger than a half of the radio wavelength at the frequency of around 50

MHz (Hocking et al., 1985). Another reason is that the winds in the mesosphere are only available during the daytime (8 LT-16 LT) in the D region (due to insufficient D region ionization during nighttime) (Rao et al., 2014). Actually, if the time range is limited in the daytime, the maximum data acquisition of the high mode is more than 50%. The analysis of the data acquisition rate indicates that the Wuhan MST radar can receive the backscattered echoes from the troposphere, stratosphere and mesosphere effectively.

3.3 Tropospheric and low stratospheric observation
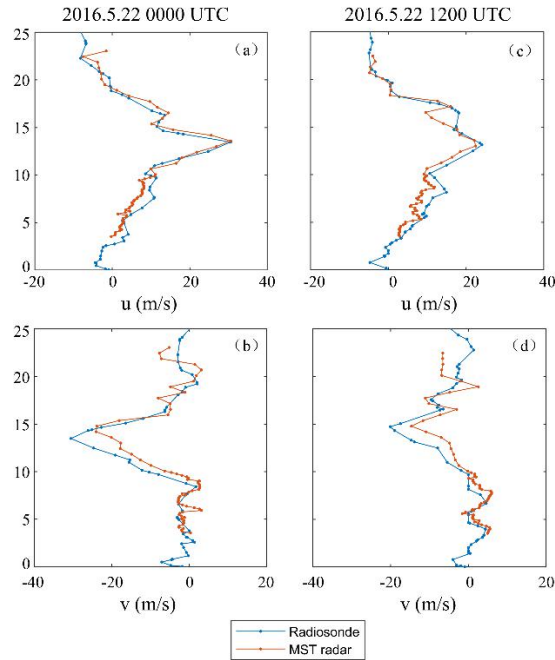
Figure 9. The zonal (u) and meridional (v) winds at heights of 3.5-25 km observed by the Wuhan MST radar (red lines) and the radiosonde (blue lines) at 00 UT (a, b) and 12 UT (c, d) on 22 May 2016.

In order to verify the validity of the wind measurements in the height ranges of 3.5-25 km, simultaneous observations obtained from the radiosonde were compared with the Wuhan MST radar observations. The radiosonde launch site (30.6°N, 114.1°E) is about 120 km away from the Wuhan MST radar, and the radiosonde was launched at 00 UT and 12 UT on 22 May 2016. It took about an hour for the balloon to rise up to 25 km, while the repetition period of the Wuhan MST radar is 30 min. Therefore, after the balloon was launched, the following two periods of the Wuhan MST radar data were averaged to compare with the data from the radiosonde.

Note that since the balloon was detected at regular intervals by the tracking radar, the height resolution of the radiosonde is not uniform. Fig. 9 shows the comparison of the zonal and meridional winds obtained by the Wuhan MST radar and the radiosonde launched at 00 UT and 12 UT on 22 May 2016. In these figures and throughout the paper, the positive zonal

component corresponds to eastward wind, while the positive meridional component corresponds to northward wind. The zonal wind profiles are in good agreement in the altitude ranges of 3.5 to 23 km. The meridional wind profiles also show good agreement at most altitudes, but the winds observed by the Wuhan MST radar are weaker around the height of 14 km. The small discrepancies at some heights could be attributed to the variations of atmospheric activities at different temporal and spatial scales, and the different measurement principles and errors in both instruments are also significant reasons (Belu et al., 2010; Hocking et al., 2001).
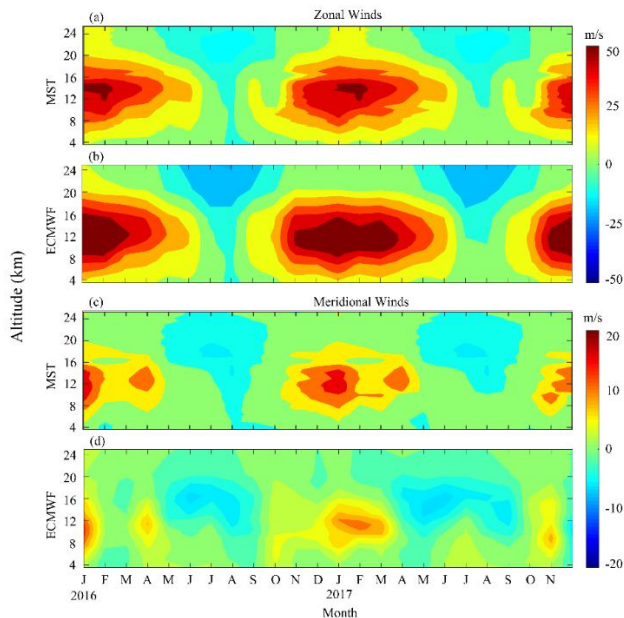
Figure 10. The contour plots of the monthly mean zonal (a) and meridional (c) winds in the troposphere and low stratosphere observed by the Wuhan MST radar during Jan 2016-Dec 2017. ERA-interim model-estimated monthly mean zonal (b) and meridional (d) winds for the Wuhan region during the same period

Fig. 10 shows the contour plots of the monthly mean zonal and meridional winds in the troposphere and low stratosphere from the Wuhan MST radar and the ERA-interim. The observed mean winds are compared with the ERA-interim. ERA-interim is one generation of European Centre for Medium-Range Weather Forecasts (ECMWF) global atmospheric reanalysis product, which offers a good quality atmospheric wind with a 6 hour temporal resolution and 3° ×3°, 0.125° ×0.125° latitude-longitude (Dee et al., 2011; Houchi et al., 2010). The dataset of monthly means of daily means is applied for the present study, which is produced by the average of the four main synoptic monthly means at 00, 06, 12, and 18 UTC (Berrisford et al., 2009).

It can be seen from Fig. 10(a) and Fig. 10(b) that the mean zonal wind observed by the Wuhan MST radar captures the major feature of the ERA-interim, which shows a clear annual oscillation with one westward jet and one eastward jet every year. The eastward jet occurs from September to June below ~20 km, and the westward jet occurs from May to October above ~20 km. The observed zonal winds in the eastward jet are ~10 m/s weaker than the ERA-interim reanalysis. The

maximum magnitudes of the westward jet from the observation and the reanalysis are ~14 m/s and ~20 m/s, respectively. As
325   shown in Fig. 10(c) and Fig. 10(d), compared to the zonal winds, the meridional winds show larger discrepancies between
the observation and the reanalysis. There are one northward jet and one southward jet exhibited in the observed mean
meridional winds every year. The northward jet occurs from November to April below ~18 km, and the southward jet occurs
from May to September above ~18 km. In the ERA-interim, the southward jets are extended in the two years. Especially in
2017, the southward jet occurs from April to October, and extends down to the low height in April and May. According to
330   the height resolution of the reanalysis data, the winds at altitudes of 3.48, 4.42, 4.94, 5.5, 6.71, 7.38, 8.81, 9.59, 10.42, 11.29,
12.21, 13.19, 15.33, 16.5, 19.05, 20.44, and 24.9 km from the Wuhan MST radar and the ERA-interim are analyzed. The
correlation coefficients of 0.96 (zonal) and 0.7 (meridional) indicate the zonal winds have a more consistent trend, and the
root mean square errors (RMSE) of 9.3 (zonal) and 4 (meridional) indicate the meridional winds have a smaller deviation.
Therefore, the larger correlation coefficient of the zonal winds may be attributed to the larger dynamic range. In conclusion,
335   the Wuhan MST radar can measure the zonal and meridional winds in the troposphere and low stratosphere effectively.

3.4 Mesospheric observation
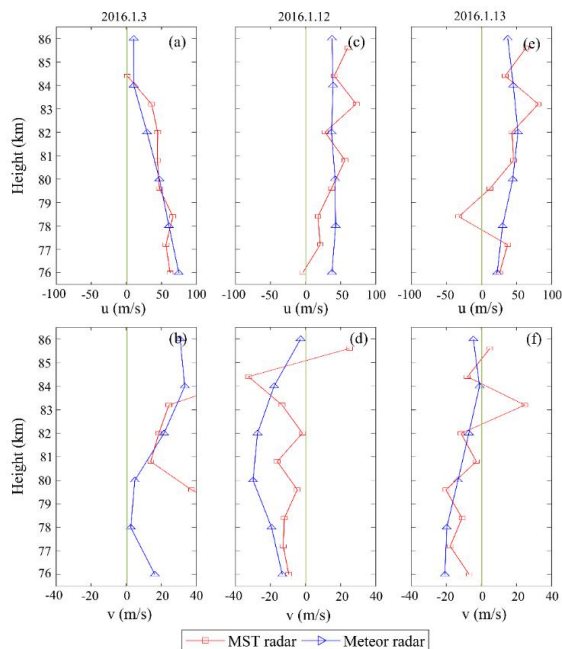
Figure 11. The daily mean zonal (u) and meridional (v) winds at heights of 76 to 86 km observed by the Wuhan MST radar (red lines) and
the Wuhan meteor radar (blue lines) on 3 January 2016 (a, b), 12 January 2016 (c, d) and 13 January 2016 (e, f).

340

In order to verify the validity of the mesospheric wind measurements, simultaneous observations obtained from the meteor
radar at Wuhan were compared with the Wuhan MST radar observations. The Wuhan meteor radar (30.6°N, 114.4°E) is
about 120 km away from the Wuhan MST radar, which is an all-sky interferometric broadband radar system with a peak

power of 7.5 kW and a frequency of 38.7 MHz (Xiong et al., 2004; Zhao et al., 2005). The averaging of daytime (8 LT-16
345 LT) observations was used as the daily mean wind estimation for the Wuhan MST radar, while the 24 hours average was
used for the Wuhan meteor radar. Because of the effect of diurnal variations, the estimated mean winds of the Wuhan MST
may be biased less than 5 m/s compared with that of the Wuhan meteor radar below 85-90 km (Nakamura et al., 1996).
Considering the observation height range of the two radars, the comparison range was set at heights of 76 to 86 km.

Fig. 11 shows the daily mean zonal and meridional winds observed by the Wuhan MST radar and the Wuhan meteor radar
350 on 3 individual days in January 2016. Interestingly, the measurements at height of around 81 km show better agreement than
other heights, except for the meridional wind on 12 January 2016. It is because the measurements of the meteor radar are
more reliable above 80 km (Ratnam et al., 2001; Kumar et al., 2008), while the data acquisition rate of the Wuhan MST
radar is relatively high at heights of 70-85 km in the mesosphere. The zonal and meridional winds are of concordance in the
aggregate. Two reasons might result in the discrepancies between the observations of the two radars. The first one is the
355 localized gravity waves, tides or planetary waves could make the differences between them (Rao et al., 2014; Ratnam et al.,
2001). The second is that the low data acquisition rate of the Wuhan MST radar in the mesosphere could lead to the
fluctuations of the daily mean data, which shows the sudden changes of the MST radar measurements at some heights.
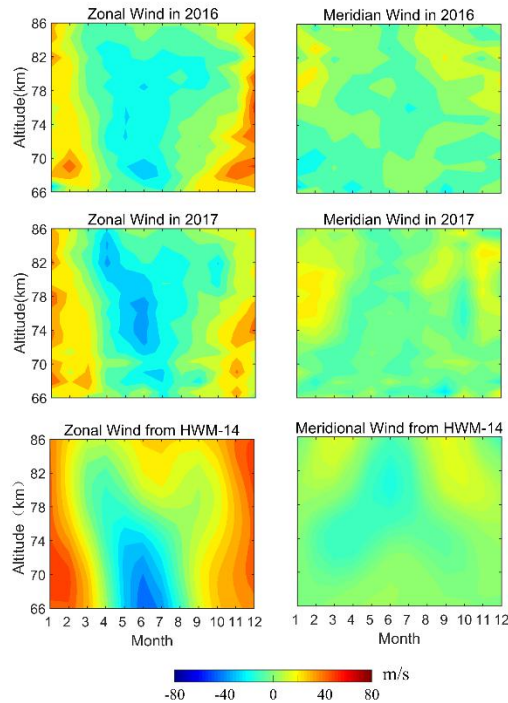
Figure 12. The contour plots of the monthly mean zonal (left) and meridional (right) winds in the mesosphere observed by the Wuhan
360 MST radar during Jan 2016-Dec 2016 and Jan 2017-Dec 2017. HWM-14 model-estimated winds (third row) for Wuhan region during the
same period.

Fig. 12 shows contour plots of the monthly mean zonal and meridional winds from the MST radar and HWM-14. The observed mean winds are compared with the Horizontal Wind Model-14 (HWM-14). HWN-14 is an empirical model describes the atmosphere's vector wind fields from the surface to the exobase (~450 km) as a function of latitude, longitude, altitude, day of year, and time of day, which is the upgraded version of HWM-07 (Drob et al., 2015).

As shown in left panels of Fig. 12, Wuhan MST radar zonal winds clearly show strong seasonal variations in 2016 and 2017. In general, the trends of the observational and predicted zonal winds match well, especially the reversal from eastward to westward in spring and the reversal from westward to eastward in autumn. However, HWM-14 overestimates the zonal winds in winter. Especially in Feb the magnitudes of the observational and predicted results have large differences. Many studies indicated that stronger northward and westward winds happen after the stratospheric sudden warming (SSW) events (Mbatha et al., 2010; Chau et al., 2015), and this factor is not considered in the HWM-14. The 2016 Feb SSW is a minor SSW, and the day of peak warming is on Feb 5 (Medvedeva et al., 2017). Two minor warming events happened during the winter of 2017, with two days of peak warming on Feb 2 and 26 (Eswaraiah et al, 2019). The SSW events happened during the observation period may influence the mean winds in the mesosphere. Hence, the stronger westward winds may result in smaller mean zonal winds during winter. Weakening and reversal in zonal winds observed between Jan and Feb can be found in Fig. S1 of the supplement. Moreover, the differences of the zonal winds in summer are noticed. The first difference is the reversal height in summer, which is a useful index for the mesopause. The wind shear around 78 km is prominent during the summer from the HWM-14. Meanwhile, the reversal height observed by the Wuhan MST radar is about 84-85 km, which is consistent with the result observed by the MU radar at similar altitude (Namboothiri et al., 1999). Further study may be needed to analyze the difference. The second difference is the westward jet (the bluer region) occurred in summer. There are some differences of the westward jet between the observations and predictions in occurrence time and height, which could be due to interannual variability. As seen from right panels of Fig. 12, it appears that the observational meridional winds of 2016 and 2017 have the same trend as the predicted results. They all have one northward jet occurred above ~75 km in the period from August to April, but the observational results are larger than the predicted results in winter because of the stronger northward winds during the SSW events. In general, the Wuhan MST radar wind measurements of the mesosphere are in agreement with the HWM-14 predictions in trend.

4 Conclusion

The technical features of the Wuhan MST radar are described in this paper. We use the TR modules and digital receiver with smart structure, and reasonable feeding network, to realize the beam steering for three-dimensional wind field measurements. Wind observations of the Wuhan MST radar are compared with other instruments and related models for validation, and the results are summarized as follows:

1. Compared with the radiosonde (120 km away) and the ERA-interim, the zonal and meridional winds are in good agreement at heights of 3.5-25 km, and large discrepancies in meridional winds could be due to the temporal and spatial differences.

2. The daily mean zonal and meridional winds are in good agreement at heights of 76 to 86 km with the Wuhan meteor radar (120 km away), and the measurements at height of around 81 km show better agreement than other heights.

3. The monthly mean zonal and meridional winds are in agreement with the HWM in trend at heights of 66 to 86 km. The amplitudes of the observational results are different from that of the predicted results in winter, and it could be due to the influence of SSW events.

The comparisons indicate that the Wuhan MST radar is an effective tool to measure the three-dimensional wind fields of the MST region. These results encourage us to do more for the improvements, such as improving the data acquisition of the high mode, and correcting the nominal zenith angle for the aspect sensitivity. In the future, we will use the Wuhan MST radar to study precipitation, gravity waves, and stratosphere-troposphere exchange processes during typhoon, cold front or other events, as well as the dynamics of the mesosphere.

Data availability. Wuhan MST radar data can be downloaded at http://159.226.22.74/.

Author contributions. LQ prepared the main part of the paper and performed the statistical analysis. GC is the project leader of the Wuhan MST radar and supported the preparation of the paper. SZ supervised the paper writing. QY implemented the construction work. The measurements were led by WG and FC. WZ and HZ helped with the statistical analysis of Wuhan MST radar. MS and EL provided valuable suggestion for data processing. The data analysis was supported by XC and HS. HZ and LZ edited the article.

Competing interests. The authors declare that they have no conflict of interest.

Acknowledgements. The authors would like to acknowledge for the use of Wuhan MST radar data from the Chinese Meridian Project. This work is supported by the Natural Science Foundation of Zhejiang Province under Grant LQ20D040001, by the Chinese Meridian Project and National Natural Science Foundation of China under Grant 41722404.

References

Anandan V. K., Reddy G. R., Rao P. B.: Spectral analysis of atmospheric radar signal using higher order spectral estimation technique, IEEE Trans. Geosci. Remote Sens., 39, 1890-1895, doi: 10.1109/36.951079, 2001.

Balsley B. B., Ecklund W. L., Carter D. A., et al.: The MST radar at Poker Flat, Alaska, Radio Sci., 15, 213–223, doi: 10.1029/RS015i002p00213, 1980.

425 Belu R. G., Hocking W. K., Donaldson N., et al.: Comparisons of CLOVAR windprofiler horizontal winds with radiosondes and CMC regional analyses, Atmos. Ocean, 39, 107-126, doi: 10.1080/07055900.2001.9649669, 2010.

Berrisford P., et al.: The ERA-Interim Archive, ERA Report Series, 2009.

Chau J. L., Hoffmann P., Pedatella N. M., et al.: Upper mesospheric lunar tides over middle and high latitudes during sudden stratospheric warming events, J. Geophys. Res., 120, 3084-3096, doi: 10.1002/2015JA020998, 2015.

430 Chen F., Chen G., et al.: High-resolution Beijing mesosphere-stratosphere-troposphere (MST) radar detection of tropopause structure and variability over Xianghe (39.75°N, 116.96°E), China, Ann. Geophys., 37, 631-643, doi: 10.5194/angeo-37-631-2019, 2019.

Chen G., Cui X., Chen F., et al.: MST Radars of Chinese Meridian Project: System Description and Atmospheric Wind Measurement, IEEE Trans. Geosci. Remote Sens., 54, 4513-4523, doi: 10.1109/TGRS.2016.2543507, 2016.

435 Chilson P. B., Kirkwood S., Nilsson A.: The Esrange MST radar: A brief introduction and procedure for range validation using balloons, Radio Sci., 34, 427–436, doi:10.1029/1998rs900023, 1999.

Chu Y., Yang K.: Reconstruction of spatial structure of thin layer in sporadic E region by using VHF coherent scatter radar, Radio Sci., 44, RS5003, doi: 10.1029/2008RS003911, 2009.

Dee D. P., et al.: The ERA-Interim reanalysis: configuration and performance of the data assimilation system, Q. J. R.
440 Meteorol. Soc., 137, 553-597, doi: 10.1002/qj.828, 2011.

Drob D.P., Emmert J. T., Meriwether J. W., et al.: An update to the Horizontal Wind Model (HWM): The quiet time thermosphere, Earth and Space Science, 2, 301-319, doi: 10.1002/2014EA000089, 2015.

Eswaraiah S., et al.: Advanced meteor radar observations of mesospheric dynamics during 2017 minor SSW over the tropical region, advances in Space Research, 64, 1940-1947, doi: 10.1016/j.asr.2019.05.039, 2019.

445 Fukao S., Tsuda T., Sato T., Kato S., Wakasugi K., and Makihira T.: The mu radar with an active phased array system: 1. Antenna and power amplifiers," Radio Sci., 20, 1155-1168, doi: 10.1029/rs020i006p01155, 1985.

Fukao S., Hashiguchi H., Yamamoto M., et al.: Equatorial Atmosphere Radar (EAR): System description and first results, Radio Sci., 38, 19-1-19-17, doi: 10.1029/2002RS002767, 2003.

Green J. L., Gage K. S., and Van Zandt T. E.: Atmospheric measurements by VHF pulsed Doppler radar, IEEE Trans.
450 Geosci. Electron., GE-17, 262–280, doi:10.1109/TGE.1979.294655, 1979.

Hocking W. K.: Measurement of turbulent energy dissipation rates in the middle atmosphere by radar techniques: A review, Radio Sci., 20, 1403-1422, doi: 10.1029/rs020i006p01403, 1985.

Hocking W. K.: VHF tropospheric scatterer anisotropy at Resolute Bay and its implications for tropospheric radar-derived wind accuracies, Radio Sci., 36, 1777-1793, doi: 10.1029/2000rs001002, 2001.

455 Hocking A. A.: A review of Mesosphere–Stratosphere–Troposphere (MST) radar developments and studies, circa 1997–2008, J. Atmos. sci., 73, 848–882, doi:10.1016/j.jastp.2010.12.009, 2011.

Houchi K., Stoffelen A., Marseille G. J., et al.: Comparison of wind and wind shear climatologies derived from high-resolution radiosondes and the ECMWF model, J. Geophys. Res., 115, D22123, doi: 10.1029/2009jd013196, 2010.

460 Hooper D. A., et al.: Renovation of the Aberystwyth MST radar: evaluation, in: Proceedings of the Thirteenth International Workshop on Technical and Scientific Aspects of MST Radar, Leibniz-Institute of Atmospheric Physics at the Rostock University, Kühlungsborn, Germany, 86–90, 2013.

Kawahigashi H., et al.: History of Development of the MU (Middle and Upper Atmosphere) Radar, the First Large-Scale Atmospheric Radar with Two-Dimensional Active Phased Array Antenna System, 2017 IEEE HISTory of ELectrotechnolgy CONference (HISTELCON), Kobe, 47-52, doi: 10.1109/HISTELCON.2017.8535930, 2017.

465 Kumar G. K., Ratnam M. V., Patra A. K., et al.: Climatology of low-latitude mesospheric echo characteristics observed by Indian mesosphere, stratosphere, and troposphere radar, J. Geophys. Res., 112, D06109, doi: 10.1029/2006JD007609, 2007.

Kumar G. K., Ratnam M. V., Patra A. K., et al.: Low-latitude mesospheric mean winds observed by Gadanki mesosphere-stratosphere-troposphere (MST) radar and comparison with rocket, High Resolution Doppler Imager (HRDI), and MF
470 radar measurements and HWM93, J. Geophys. Res., 113, D19117, doi: 10.1029/2008JD009862, 2008.

Kumar S., Rao T. N., and Radhakrishna B.: Identification and Separation of Turbulence Echo From the Multipeaked VHF Radar Spectra During Precipitation, IEEE Trans. Geosci. Remote Sens., 57, 5729 – 5737, doi: 10.1109/TGRS.2019.2901832, 2019.

Latteck R., Singer W., Rapp M., et al.: MAARSY: The new MST radar on Andøya—System description and first results,
475 Radio Sci., 47, 222-237, doi: 10.1029/2011RS004775, 2012.

Mbatha N., Sivakumar V., Malinga S. B., et al.: Study on the impact of sudden stratosphere warming in the upper mesosphere-lower thermosphere regions using satellite and HF radar measurements, Amos. Chem. Phys., 10, 3397-3404, doi: 10.5194/acp-10-3397-2010, 2010.

Medvedeva I., Ratovsky K.: Effects of the 2016 February minor sudden stratospheric warming on the MLT and ionosphere
480 over Eastern Siberia, Journal of Atmospheric and Solar Terrestrial Physics, 180, 116-125, doi: 10.1016/j.jastp.2017.09.007, 2017.

Namboothiri S. P., Tsuda T., Nakamura T.: Interannual variability of mesospheric mean winds observed with the MU radar, J. Atmos. sci., 61, 1111-1122, doi: 10.1016/S1364-6826(99)00076-0, 1999.

Nakamura T., Tsuda T., Fukao S.: Mean winds at 60–90 km observed with the MU radar (35°N), J. Atmos. sci., 58, 655-660,
485 doi: 10.1016/0021-9169(95)00064-X, 1996.

Ratnam M. V., Rao D. N., Rao T. N., et al.: Mean winds observed with Indian MST radar over tropical mesosphere and comparison with various techniques, Ann. Geophys., 19, 1027-1038, doi: 10.5194/angeo-19-1027-2001, 2001.

Rao P. B., Jain A. R., Kishore P., Balamuralidhar P., Damle S. H., and Viswanathan G.: Indian MST radar 1. System description and sample vector wind measurements in ST mode, Radio Sci., 30, 1125-1138, doi: 10.1029/95RS00787, 1995.
490 Rao Q., Hashiguchi H., Fukao S.: Study on ground clutter prevention fences for boundary layer radars, Radio Sci., 38, 13-1–13-15, doi: 10.1029/2001rs002489, 2003.

Rao S. V. B., Eswaraiah S., Ratnam M. V., et al.: Advanced meteor radar installed at Tirupati: System details and comparison with different radars, J. Geophys. Res., 119, 11893-11904, doi: 10.1002/2014JD021781, 2014.

Rottger J., Liu C. H., Chao J. K., et al.: The Chung-Li VHF radar: Technical layout and a summary of initial results, Radio Sci., 25, 487-502, doi: 10.1029/RS025i004p00487, 1990.

Sato K., Tsutsumi M., Sato T., et al.: Program of the Antarctic Syowa MST/IS radar (PANSY), J. Atmos. sci., 118, 2–15, doi: 10.1016/j.jastp.2013.08.022, 2014.

Schmidt G., Ruster R., Czechowsky P.: Complementary Code and Digital Filtering for Detection of Weak VHF Radar Signals from the Mesosphere, IEEE Trans. Geosci. Electron., 17, 154–161, doi: 10.1109/tge.1979.294643, 1979.

Vaughan G.: The UK MST radar, Weather, 57, 69-73, doi: 10.1002/wea.6080570206, 2002.

Wang C.: Development of the Chinese Meridian Project, Chin. J. Space. Sci., 30, 382–384, doi: 10.1360/972009-470, 2010.

Woodman R. F. and Guillen A.: Radar observations of winds and turbulence in the stratosphere and mesosphere, J. Atmos. sci., 31, 493–505, doi:10.1175/1520-0469(1974)031<0493:ROOWAT>2.0.CO;2, 1974.

Xiong J. G., Wan W., Ning B., et al.: First results of the tidal structure in the MLT revealed by Wuhan Meteor Radar (30°40′N, 114°30′E), J. Atmos. sci., 66, 675-682, doi: 10.1016/j.jastp.2004.01.018, 2004.

Zhao G., Liu L., et al.: "Seasonal behavior of meteor radar winds over Wuhan," Earth, Planets and Space, 57, 393-398, doi: 10.1186/BF03351806, 2005.